Quantum Well Infrared Photodetectors for Low Background Applications

S. D. Gunapala, S. V. Bandara, A. Singh[a], J. K. Liu, E. M. Luong,
J. M. Mumolo, M. J. McKelvey

Center for Space Microelectronics Technology, Jet Propulsion Laboratory, California Institute of Technology, Pasadena, CA 91109

[a]Air Force Research Laboratory
Kirtland Air Force Base, NM 87117

ABSTRACT

High performance long-wavelength GaAs/$Al_xGa_{1-x}As$ quantum well infrared photodetectors for low background applications have been demonstrated. This is the first theoretical analysis of quantum well infrared photodetectors for low background applications and the detectivity D* of $6x10^{13}$ cm$\sqrt{Hz}$/W has been achieved at T = 40 K with 2 x 10^9 photons/cm^2/sec background. In addition, this paper describes the demonstration of mid-wavelength/long-wavelength dualband quantum well infrared photodetectors and long-wavelength/very long-wavelength dualband quantum well infrared photodetectors in 4-26 μm wavelength region.

1. INTRODUCTION

In recent years, quantum well infrared photodetectors (QWIPs) based on III-V semiconductor hetero-structures have been extensively investigated for myriad high background applications in the fields of medicine, defense and science. Many research groups have shown impressive imaging performance at high-background conditions using large area (i.e., up to 640x486) highly uniform focal plane arrays (FPAs)[1-4]. It is quite clear now, the mature GaAs/AlGaAs growth and processing technologies are the key to the success of GaAs based QWIP FPAs. Furthermore, QWIPs offer low cost per pixel and large format FPAs due to the availability of large highly uniform 6 inch epitaxially grown GaAs/AlGaAs wafers. In addition, III-V based QWIPs tuned to detect light at wavelengths from 3 to 25 μm offer radiation hardness, stability, reliability and no 1/f noise down to very low frequencies (i.e., less than a one tenth of a Hertz).

In this paper, we discuss the demonstration of high performance QWIPs for low background applications, the demonstration of mid-wavelength/long-wavelength dualband QWIPs, and long-wavelength/very long-wavelength dualband QWIPs in 4-26 μm wavelength region. Improving QWIP performance depends largely on minimizing the Shott noise of the dark current (the current that flows through a biased detector in the dark, i.e., with no photons impinging on it) and improving the quantum efficiency. In order to analyze the dark current of a QWIP which has a intersubband absorption peak in long-wavelength region, we first calculated the effective number of electrons[5,6] n(V) which are thermally excited into the continuum transport states, as a function of bias voltage V, using the following expression.

$$n(V) = \left(\frac{m^*}{\pi\hbar^2 L_p}\right)\int_{E_0}^{\infty} f(E)T(E,V)dE \qquad (1)$$

The first factor containing the effective mass m* represents the average three dimensional density of states. Where L_p is the superlattice period, f(E) is the Fermi factor $f(E) = [1 + \exp(E-E_0-E_F)/KT]^{-1}$, E_0 is the bound state energy, E_F is the two-dimensional Fermi energy, E is the energy of the electron, and T(E,V) is the tunneling current transmission factor which is obtained by using WKB approximation to a biased quantum well. In equation 1, the effective number of electrons above the barrier account for thermionic contribution and the number of electrons below the barrier account for thermionic assisted tunneling and tunneling contribution of the dark current. Then the bias-dependent dark current $I_d(V)$ was calculated, using $I_d(V) = eAn(V)v(V)$, where v(V) is the average transport velocity , A is the device area, and e is the electronic charge. The average transport velocity was calculated using $v(V) = \mu F[1 + (\mu F/v_s)^2]^{-1/2}$, where μ is the mobility, F is the electric field, and vs is the saturated drift velocity. In order to obtain bias-dependent dark current at T = 60K, μ = 1200 cm^2/Vs and v_s =

5.5 x 10^6 cm/s was used. Fig. 1 shows the T = 60K dark current due to thermionic emission, total dark current (thermionic + thermionic assisted tunneling + tunneling), and experimental dark current of a QWIP sample which has cutoff wavelength λ_c = 10 μm. According to the calculations tunneling through the barriers dominates the dark current at temperatures below 30K, and at temperatures above 30 K thermionic emission into the continuum transport states dominates the dark current.

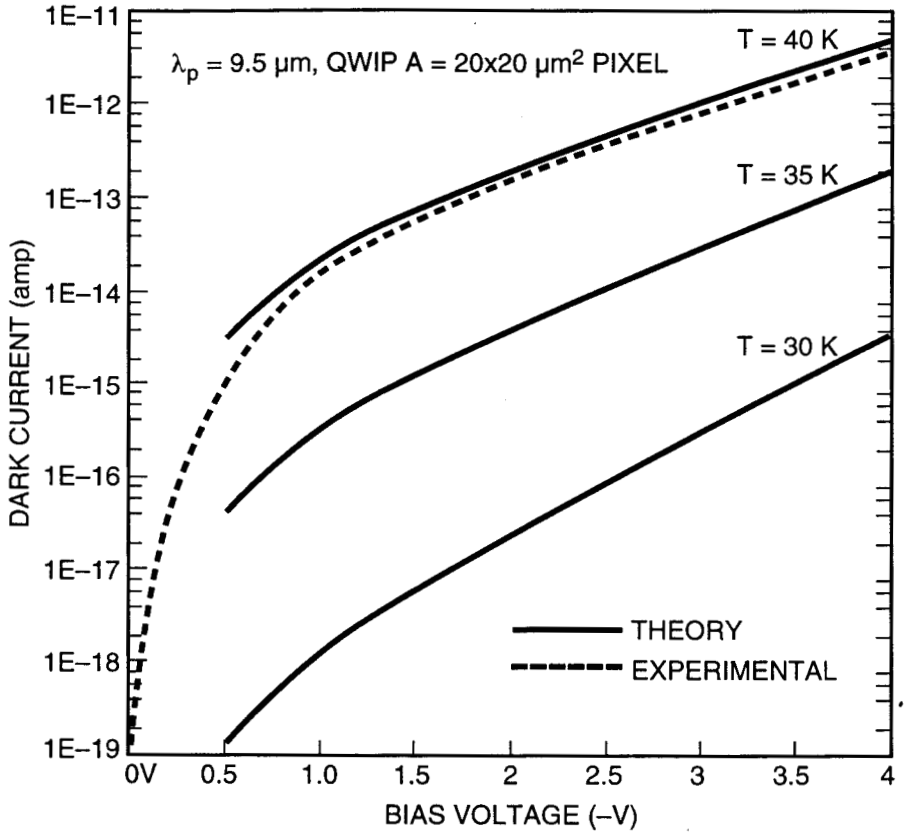

Fig. 1. Comparison of experimental (solid curves) and theoretical (dashed) dark current versus bias voltage curves at various temperatures for a 10 μm cutoff QWIP.

2. LOW BACKGROUND QWIPs

Eight n-type doped QWIP device structures were grown for this experiment. These n-doped QWIPs were grown using molecular beam epitaxy and the wells and contact layers were doped with Si. The quantum well widths L_w range from 35 to 50 Å, while the barrier widths are approximately constant at L_b = 500 Å. The Al molar fraction in the $Al_xGa_{1-x}As$ barriers varies from x = 0.24 to 0.30 (corresponding to cutoff wavelengths of λ_c = 8.3 – 10.3 μm). The photosensitive doped multiquantum-well (MQW) region (containing 25 to 50 periods) is sandwiched between similarly doped top (0.5 μm) and bottom (0.5 μm) ohmic contact layers. These structural parameters have been chosen to give a very wide variation in the QWIP absorption and transport properties. All eight QWIP samples are n-doped with intersubband infrared transition occurring between a single localized bound state in the well and a delocalized state in the continuum. Thus, the intersubband transition occurs from the bound state to a delocalized state in the continuum. In the presence of an electric field, the photoexcited carrier can be effectively swept out of the quantum well region.

All eight QWIP samples were processed into 200 μm diameter mesas (area = 3.14 x 10^{-4} cm^2) using wet chemical etching and Au/Ge ohmic contacts were evaporated onto the top and bottom contact layers. The dark current versus voltage curves for all samples were measured as a function of temperature from T = 40-70 K and Fig. 1 shows the current-voltage curve of one sample. As expected, Fig. 1 clearly shows that the T = 40 K dark current of these QWIP devices are many orders of magnitude smaller than the dark current at T = 70 K. This clearly indicates that the dark current of these devices are thermionic dominant down to 40 K and the tunneling induced dark current is insignificant.

3. RESULTS AND ANALYSIS

The responsivity spectra of all detectors were measured using a 1000 K blackbody source and a grating monochromator. The detectors were back illuminated through a 45° polished facet and their normalized responsivity spectrums are shown in Fig. 2. The responsivities of all device structures peaked in the range from 7.7 μm and 9.7 μm. The peak responsivities (R_p), spectral widths ($\Delta\lambda$), cutoff wavelengths (λ_c) and quantum efficiency photoconductive gain products (η x g) are listed in Table I. It is worth noting that hg product of sample four has increased to 17%. This is approximately a factor of 24 increase in hg product compared to hg product of our QWIP devices designed for high background and high temperature operation.

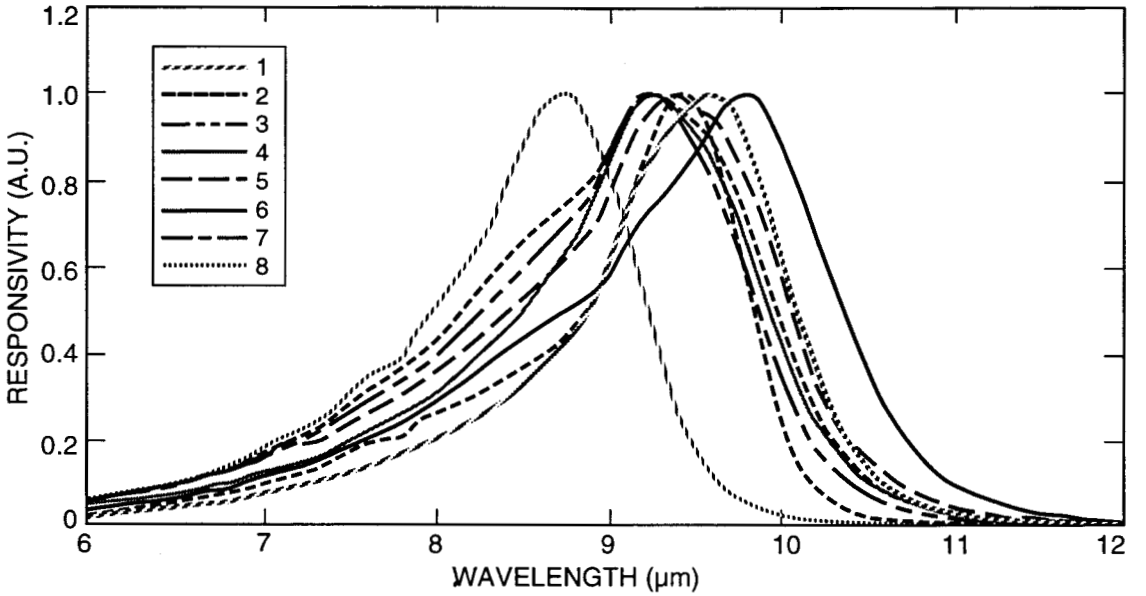

Fig. 2. Normalized responsivity spectra versus wavelength at T= 40 K for all samples.

TABLE I. Responsivity spectral parameters of all eight samples.

	Spectral Response (μm)			Device Performance (Detector Area 3.1 x 10^{-4} cm^2)		
Sample	λp	50% λ_c	Δλ	Peak Rp A/W @ 2V	Q.E. x Gain %	Dark Current @ 50K
1	9.6	10.1	1.1	0.65	8.4	1.1 E-11
2	9.4	10.1	1.6	0.61	8.0	8.0 E-11
3	9.3	9.8	1.6	0.38	5.2	2.0 E-11
4	9.3	9.8	1.2	1.26	17.0	9.0 E-11
5	9.4	10.0	1.8	0.46	6.1	1.0 E-10
6	9.7	10.3	1.5	0.54	5.3	3.0 E-10
7	8.5	8.9	1.0	0.15	2.2	1.0 E-12
8	7.7	8.3	1.3	0.34	5.5	2.5 E-12

We have compared the transport and absorption properties of sample one and four. The MQW region of sample one consists of 50 periods of 45 Å well of GaAs (doped n ~ 5 x 10^{17} cm^{-3}) and 500 Å barrier of $Al_{0.28}Ga_{0.72}As$ and sample four consists of 30 periods of 40 Å well of GaAs (doped n ~ 1 x 10^{18} cm^{-3}) and a 500 Å barrier of $Al_{0.3}Ga_{0.7}As$. The electric fields in the MQW regions of first (50 periods) and fourth (30 periods) samples can be expressed as $E_{50} = V_B/50L_P$ and $E_{30} = V_B/30L_P$, where L_P is the length of a period. Thus, for a given bias voltage the electric fields of the first and the fourth samples relate as $E_{30} = 5\ E_{50}/3$. Variation of responsivity of these two QWIP detectors as a function of bias voltage is shown in Fig. 3. Responsivity of both detectors saturate around bias V_B = -2 V. This responsivity saturation at a moderate electric fields and the spectral shapes (Fig. 3) clearly indicate that the first and the fourth samples were designed to have bound-to-

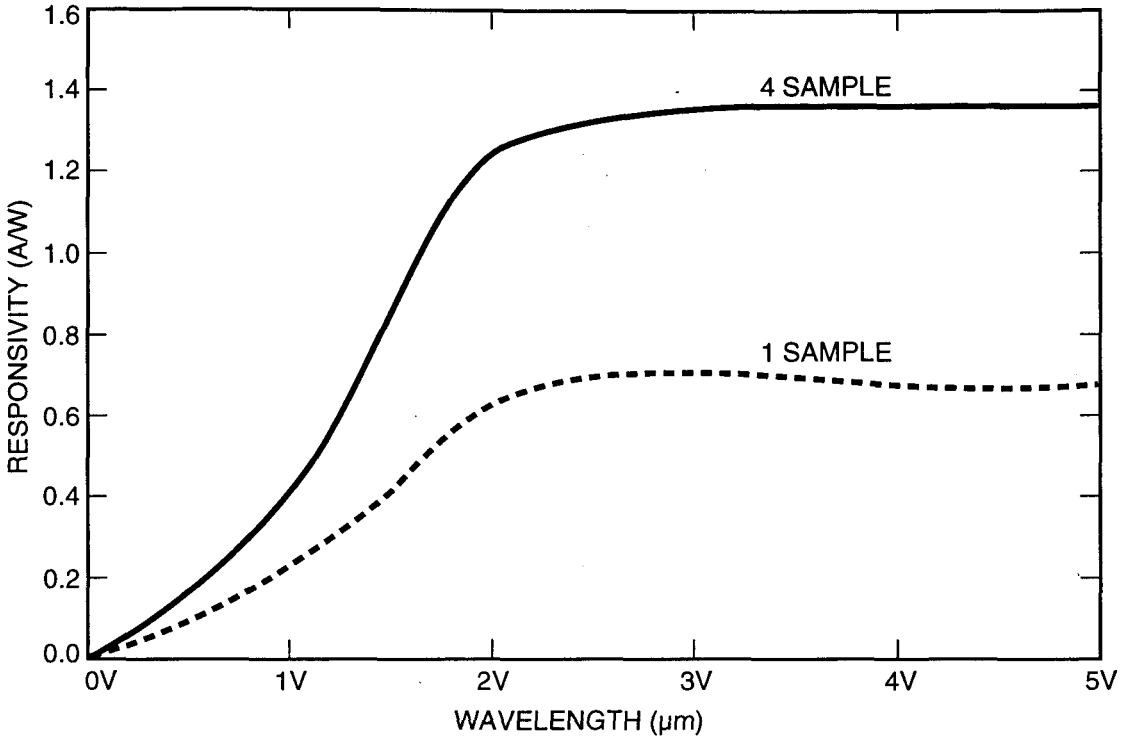

Fig. 3. Responsivity spectrums of the first (dashed) and the fourth (solid) samples measured at T = 40 K.

continuum intersubband absorption. Drift velocity of the carrier is given by $\upsilon(V_B) = \mu E/\sqrt{(1 + (\mu E/\upsilon_s)2)}$, where μ is the mobility of the carriers and υ_s is the saturated drift velocity. Therefore, at moderate bias voltages it is fair to use the approximation that $\upsilon(VB) = \upsilon_s$. Thus, photoconductive gain of the detectors is independent of V_B at saturation. Since photoconductive gain can be expressed[7] as $g = L/l_{MQW}$, where L is the hot electron mean free path and l_{MQW} is the length of MQW region of the detectors. Thus, photoconductive gains of the first (50 periods) and the fourth (30 periods) samples can be expressed as $g_{50} = L/50L_P$ and $g_{30} = L/30L_P$. Therefore, at moderate electric fields the photoconductive gains of first and fourth detectors relate as $g_{30} = 5\ g_{50}/3$. Absorption quantum efficiencies of the first and the fourth detectors relate as $\eta_{30} = 3\ \eta_{50}/5$, since in the linear absorption region quantum efficiency η can be written[8] as $\eta = N\eta_a$ where N is the number of periods and η_a is the absorption quantum efficiency per period. This leads to following expression relating absorption quantum efficiency and photoconductive gain products of the two samples,

$$\eta_{30}\, g_{30} = \eta_{50}\, g_{50} \tag{2}$$

We can assume $\eta \propto N_D$ at a given wavelength since responsivity[9] $R \propto N_D(\lambda/\Delta\lambda)$. Experimental measurement shows h50 g50 = 8%. Since the well doping of the fourth sample is twice high as the first sample $\eta_{30}\, g_{30}$ = 16%. This closely agrees with the experimentally measured value of $h_{30}\, g_{30}$ = 16.8%.

The current noise i_n was measured using a spectrum analyzer. The peak detectivity D* can now be calculated from $D^* = R\sqrt{A\Delta f}/i_n$, where A is the area of the detector and A = 27x27 μm^2. Table II shows the D* values of both device structures at various bias voltages at T = 40 K. These data clearly show that detectivities of 10 μm cutoff QWIPs reach mid 10^{13} cm$\sqrt{Hz}$/W at T = 40 K. As shown in Table II, these detectors are not showing background limited performance (BLIP) for moderately low background of 2 x 10^9 photons/cm^2/sec at T = 40 K operation. Since the dark current of these detectors are thermionically limited down to T = 30 K, these detectors should demonstrated BLIP at T = 35 K for 2 x 10^9 photons/cm^2/sec background.

4. DUALBAND (MID-WAVELENGTH AND LONG-WAVELENGTH) DETECTORS

There are several applications such as target recognition and discrimination which require monolithic mid and long wavelength dualband large area, uniform, reproducible, low cost and low 1/f noise infrared FPAs. For example, a dualband FPA camera would provide the absolute temperature of the target which is extremely important to the process of identifying

TABLE II. Responsivity, quantum efficiency, photoconductive gain, and detectivity of the first and the fourth sample at T = 40 K.

Pixel Area: 27 μm x 27 μm
Background Flux: 2 x 10^9 photons/cm^2/sec

Sample	Peak W.L. (μm)	Bias (V)	Responsivity (A/W)	Q.E. x Gain %	ABS. Q.E. @ 300K	ABS. Q.E. @ 40K	Optical Gain	Dark Current @ 40K (A)	Photo-Current (A)	Detectivity cm $Hz^{1/2}$/W
1	9.6	1.0	0.24	3.1	14.1	18.3	0.17	1.2 E-15	7.2 E-17	5.7 E+13
		2.0	0.65	8.4	14.1	18.3	0.46	2.3 E-15	1.9 E-16	6.8 E+13
		3.0	0.66	8.5	14.1	18.3	0.47	9.3 E-15	2.0 E-16	3.4 E+13
		4.0	0.68	8.8	14.1	18.3	0.48	1.4 E-14	2.1 E-16	2.8 E+13
4	9.3	1.0	0.43	5.7	17.0	22.1	0.26	7.0 E-15	1.3 E-16	3.4 E+13
		2.0	1.26	16.8	17.0	22.1	0.76	9.3 E-15	3.9 E-16	5.1 E+13
		3.0	1.35	18.0	17.0	22.1	0.81	3.5 E-14	4.2 E-16	2.7 E+13
		4.0	1.36	18.1	17.0	22.1	0.82	2.3 E-13	4.2 E-16	1.1 E+13

temperature difference between targets, war heads and decoys. The GaAs based QWIP is a potential candidate for development of such a two-color FPAs. Until recently, the most developed and discussed two-color QWIP detector was the voltage tunable two stack QWIP. This device structure consists of two QWIP structures, one tuned for mid-wavelength detection and the other stack tuned for long-wavelength detection. This device structure utilizes the advantage of formation of electric field domains to select the response of one or the other detector[10,11] (MQW region). The difficulties associated with this type of two-color QWIP FPA are that these detectors need two different voltages to operate and long-wavelength sensitive segment of the device needs very high bias voltage (> 8 V) to switch on the long-wavelength infrared (LWIR) detection. The other disadvantage is the voltage tunable scheme will not provide simultaneous data from both wavelength bands.

Therefore, we have developed a following QWIP device structure which can be processed in to dualband QWIP FPAs with dual or triple contacts to access the CMOS readout multiplexer[12,13]. The device structure consists of a stack of 30 periods of mid-wavelength infrared (MWIR) QWIP structure and another stack of 10 periods of LWIR QWIP structure separated by a heavily doped 0.5 mm thick intermediate GaAs contact layer. The first stack (LWIR) consist of 10 periods of 500 Å $Al_xGa_{1-x}As$ barrier and a GaAs well. This LWIR QWIP structure has been designed to have a bound-to-quasibound intersubband absorption peak at 8.5 μm, since the dark current of the device structure is expected to dominate by the longer wavelength portion of the device structure. The second stack (MWIR) consist of 30 periods of 500 Å $Al_xGa_{1-x}As$ barrier and narrow $In_xGa_{1-x}As$ well sandwiched between two thin layers of GaAs. This MWIR QWIP structure has been designed to have a bound-to-continuum intersubband absorption peak at 4.2 μm, since photo current and dark current of the MWIR device structure is relatively small compared to the LWIR portion of the device structure. This two-color QWIP structure is then sandwiched between 0.5 μm GaAs top and bottom contact layers doped n = $5x10^{17}$ cm^{-3}, and has been grown on a semi-insulating GaAs substrate by MBE. Then a 1.0 μm thick GaAs cap layer on top of a 300 Å $Al_{0.3}Ga_{0.7}As$ stop-etch layer has to be grown in situ on top of the device structure to fabricate the light coupling optical cavity.

The detectors were back illuminated through a 45° polished facet as described earlier and a simultaneously measured responsivity spectrum of vertically integrated dualband QWIP is shown in Fig. 4. The responsivity of the MWIR detector peaks at 4.4 μm and the peak responsivity (R_p) of the detector is 140 mA/W at bias V_B = -3 V. The spectral width and the cutoff wavelength of the MWIR detector are $\Delta\lambda/\lambda$ = 20% and λ_c = 5 μm respectively. The responsivity of the LWIR detector peaks at 8.8 μm and the peak responsivity (R_p) of the detector is 150 mA/W at bias V_B = -1.2 V. The spectral width and the cutoff wavelength of the LWIR detector are $\Delta\lambda/\lambda$ = 14% and λ_c = 9.4 μm respectively. The measured absolute peak responsivity of both MWIR and LWIR detectors are small, up to about V_B = -0.5 V. Beyond that it increase nearly linearly with bias in both MWIR and LWIR detectors reaching R_P = 210 and 440 mA/W respectively at V_B = -4 V. This type of behavior of responsivity versus bias is typical for a bound-to-continuum and bound-to-quasibound QWIPs in MWIR and LWIR bands respectively. The peak quantum efficiency of MWIR and LWIR detectors were 2.6% and 16.4% respectively at operating biases indicated in Fig. 4 for a 45° double pass. The lower quantum efficiency of MWIR detector is due to the lower well doping density (5 x 10^{17} cm^{-3}). The peak detectivities of both MWIR and LWIR detectors were estimated at different operating temperature and bias voltages using experimentally measured noise currents and results are shown in Figs. 5 and 6.

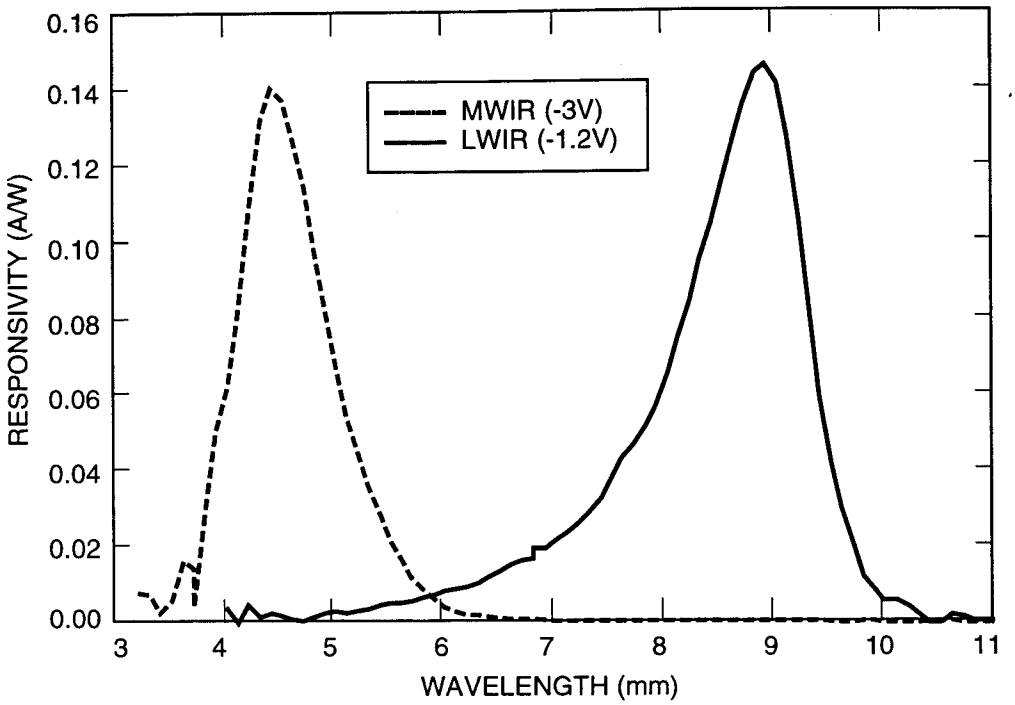

Fig. 4. Simultaneously measured responsivity spectrum of vertically integrated MWIR and LWIR dualband QWIP detector.

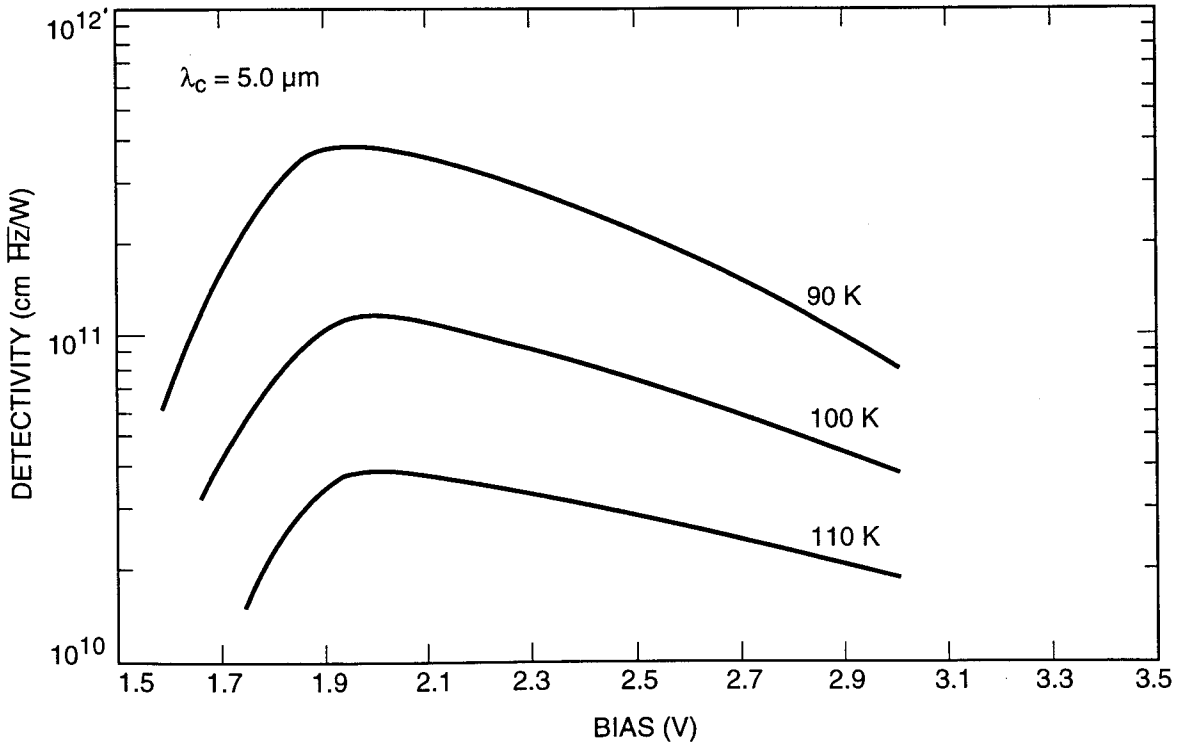

Fig. 5. Experimentally measured peak detectivity of MWIR detector as a function of bias voltage at three different operating temperatures.

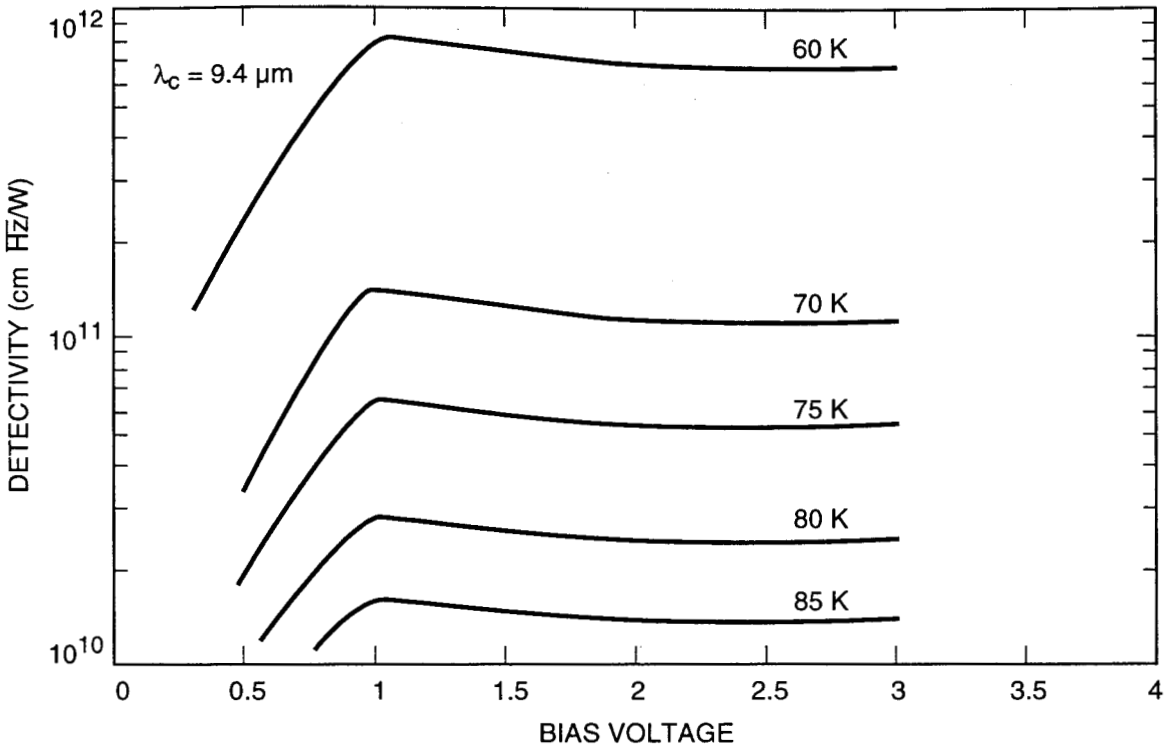

Fig. 6. Experimentally measured peak detectivity of LWIR detector as a function of bias voltage at five different operating temperatures.

5. DUALBAND (LONG-WAVELENGTH AND VERY LONG-WAVELENGTH) DETECTORS

As we discussed in the previous section of this paper, there are many target recognition and discrimination applications which require monolithic dualband large area, uniform, reproducible, low cost and low 1/f noise infrared FPAs. The general notion is that dualband target recognition and discrimination capability significantly improve with increasing wavelength separation between the two wavelength bands in consideration. Therefore, we are currently developing a 640x486 LWIR and very-long-wavelength infrared (VWIR) dualband QWIP FPA camera. Thus, we have developed a following QWIP device structure which can be processed in to dualband QWIP FPAs with dual or triple contacts to access the CMOS readout multiplexer [7,8]. Single indium bump per pixel is usable only in the case of interlace readout scheme (i.e., odd rows for one color and the even rows for the other color) which uses an existing single color CMOS readout multiplexer. The advantages of this scheme are that it provides simultaneous data readout and allows to use currently available single color CMOS readout multiplexers. However, the disadvantage is that it does not provides a full fill factor for both wavelength bands. This problem can be eliminated by fabricating (n+1) terminals (e.g., three terminals for dualband) per pixel and hybridizing with a multicolor readout having n readout cells per detector pitch, where n is the number of bands.

The device structure consists of a stack of 25 periods of LWIR QWIP structure and another stack of 25 periods of VWIR QWIP structure separated by a heavily doped 0.5 mm thick intermediate GaAs contact layer. The first stack (VWIR) consist of 25 periods of 500 Å $Al_xGa_{1-x}As$ barrier and a GaAs well. This VWIR QWIP structure has been designed to have a bound-to-quasibound intersubband absorption peak at 15 μm, since the dark current of the device structure is expected to dominate by the longer wavelength portion of the device structure. The second stack (LWIR) consist of 25 periods of 500 Å $Al_xGa_{1-x}As$ barrier and narrow GaAs well. This LWIR QWIP structure has been designed to have a bound-to-continuum intersubband absorption peak at 8.5 μm, since photo current and dark current of the MWIR device structure is relatively small compared to the VWIR portion of the device structure. This whole dualband QWIP structure is then sandwiched between 0.5 μm GaAs top and bottom contact layers doped n = 5 x 10^{17} cm^{-3}, and has grown on a semi-insulating GaAs substrate by MBE. Then a 1.0 μm thick GaAs cap layer on top of a 300 Å $Al_{0.3}Ga_{0.7}As$ stop-etch layer has to be grown in situ on top of the device structure for the fabrication of light coupling optical cavity.

The detectors were back illuminated through a 45° polished facet as described earlier and a simultaneously measured responsivity spectrum of vertically integrated dualband QWIP is shown in Fig. 7. The responsivity of the LWIR detector

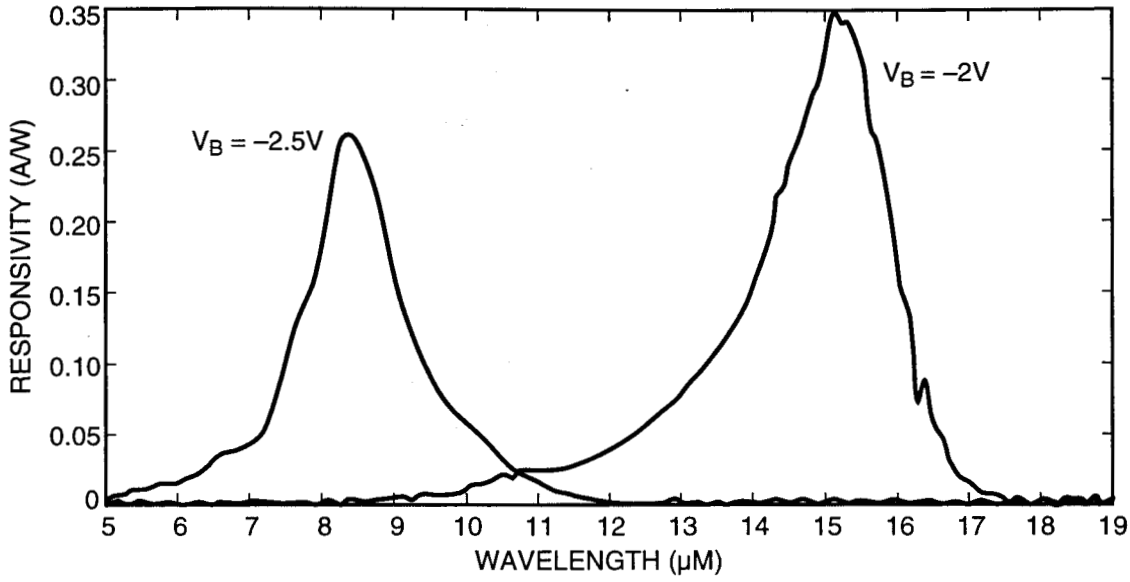

Fig. 7. Simultaneously measured responsivity spectrum of vertically integrated LWIR and VWIR dualband QWIP detector.

peaks at 8.3 μm and the peak responsivity (R_p) of the detector is 260 mA/W at bias V_B = -2.5 V. The spectral width and the cutoff wavelength of the LWIR detector are $\Delta\lambda/\lambda$ = 19% and λ_c = 9.3 μm respectively. The responsivity of the VWIR detector peaks at 15.2 μm and the peak responsivity (R_p) of the detector is 340 mA/W at bias V_B = -2.0 V. The spectral width and the cutoff wavelength of the LWIR detector are $\Delta\lambda/\lambda$ = 12% and λ_c = 15.9 μm respectively. The measured absolute peak responsivity of both LWIR and VWIR detectors are small, up to about V_B = -0.5 V. Beyond that it increase nearly linearly with bias in both LWIR and VWIR detectors.reaching R_P = 0.3 (at V_B = -2V) and 1 A/W (at V_B = -3V) respectively. This type of behavior of responsivity versus bias is typical for bound-to-continuum and bound-to-quasibound QWIPs in LWIR and VWIR bands respectively. The peak quantum efficiency of LWIR and VWIR detectors were 2.6% and 16.4% respectively at operating biases indicated in Fig. 7 for a 45° double pass. The lower quantum efficiency of LWIR detector is due to the lower well doping density (5 x 10^{17} cm^{-3}). The peak detectivities of both LWIR and VWIR detectors were estimated at different operating temperature and bias voltages using experimentally measured noise currents and results are shown in Figs. 8 and 9.

In summary, we have demonstrated that long-wavelength (λ_c = 10 μm) GaAs based QWIPs can achieve the sensitivities required for low background applications. The astronomical data obtained from a 256x256 engineering grade FPA confirm the predictions based on single element detectors. In addition, we have demonstrated MWIR:LWIR and LWIR:VWIR dualband QWIP detectors in 4 to 16 μm wavelength region.

6. ACKNOWLEDGMENTS

The research described in this paper was performed by the Center for Space Microelectronics Technology, Jet Propulsion Laboratory, California Institute of Technology, and was jointly sponsored by the JPL Director's Research and Development Fund, the Ballistic Missile Defense Organization / Innovative Science & Technology Office, the National Aeronautics and Space Administration, Office of Space Science, and the Air Force Research Laboratory.

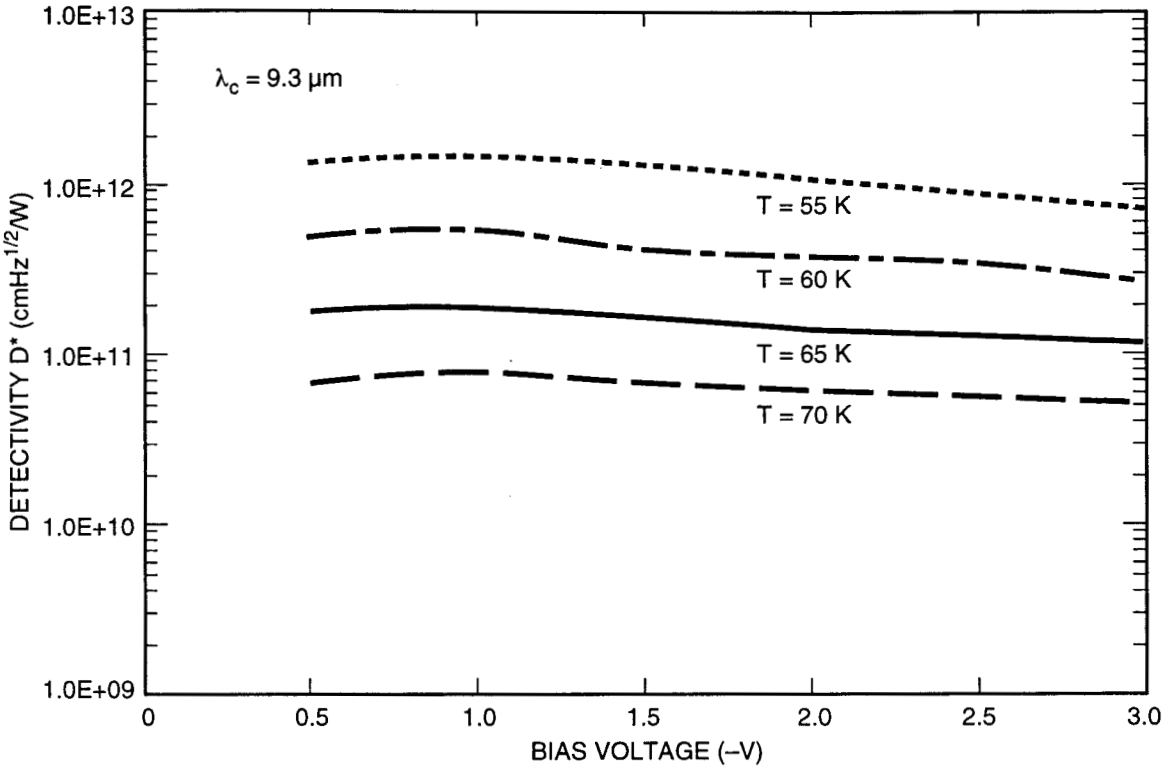

Fig. 8. Experimentally measured peak detectivity of LWIR detector as a function of bias voltage at three different operating temperatures.

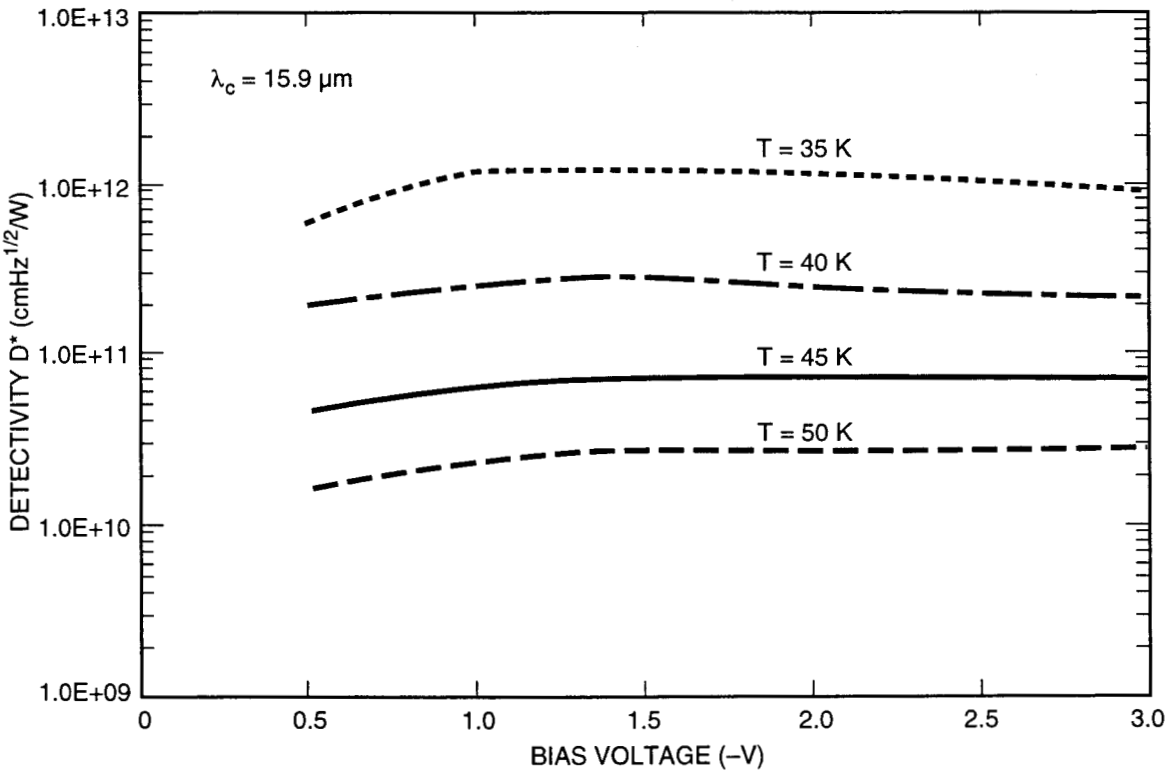

Fig. 9. Experimentally measured peak detectivity of VWIR detector as a function of bias voltage at five different operating temperatures.

7. REFERENCES

1. S. D. Gunapala, S. V. Bandara, J. K. Liu, W. Hong, M. Sundaram, R. Carralejo, C. A. Shott, P. D. Maker, and R. E. Muller, "Long-wavelength 640x484 GaAs/$Al_xGa_{1-x}As$ Quantum Well Infrared Photodetector Focal Plane Array Camera", SPIE Proceeding, IR Technology and Applications, pp. 722-727, Vol. 3061, 1997.

2. Sarath D. Gunapala, John K. Liu, Jin S. Park, Mani Sundaram, Craig A. Shott, Ted Hoelter, True-Lon Lin, S. T. Massie, Paul D. Maker, Richard E. Muller, and Gabby Sarusi" 9 μm Cutoff 256x256 GaAs/$Al_xGa_{1-x}As$ Quantum Well Infrared Photodetector Hand-Held Camera", IEEE Trans. Electron Devices, **44**, pp. 51-57, 1997.

3. J. Y. Andersson, J. Alverbro, J. Borglind, P. Helander, H. Martijn, and M. Ostlund, "320x240 Pixels Quantum Well Infrared Photodetector (QWIP) Array for Thermal Imaging: Fabrication and Evaluation", SPIE Proceeding, IR Technology and Applications, pp. 740-748, Vol. 3061, 1997.

4. W. A. Beck, T. S. Faska, J. W. Little, J. Albritton, and M. Sensiper, *Proceedings of the Second International Symposium on 2-20 μm Wavelength Infrared Detectors and Arrays: Physics and Applications*, October 10-12, 1994, Miami Beach, Florida.

5. S. D. Gunapala and K. M. S. V. Bandara, Physics of Thin Films, Academic Press, **21**, 113 (1995).

6. B. F. Levine, C. G. Bethea, G. Hasnain, V. O. Shen, E. Pelve, R. R. Abbott, and S. J. Hsieh, Appl. Phys. Lett., **56**, 851 (1990).

7. G. Hasnain, B. F. Levine, S. Gunapala, and N. Chand, Appl. Phys. Lett. **57**, 608 (1990).

8. B. F. Levine, A. Zussman, S. D. Gunapala, M. T. Asom, J. M. Kuo, and W. S. Hobson, J. Appl. Phys. **72**, 4429 (1992).

9. S. D. Gunapala, B. F. Levine, L. Pfeiffer, and K. West, J. Appl. Phys. **69**, 6517 (1990).

10. I. Grave, A. Shakouri, N. Kuze, and A. Yariv, "Control of electric field domain formation in multiquantum well structures", Appl. Phys. Lett. **63**, 1101 (1993).

11. Ting Mei, G. Karunasiri, and S. J. Chua, "Two-color infrared detection using intersubband transitions in multiple step quantum wells with superlattice barriers", Appl. Phys. Lett. **71**, 2017 (1997).

12. Ph. Bois, E. Costard, J. Y. Duboz, J. Nagle, E. Rosencher, and B. Vinter, "Optimized multiquantum well infrared detectors ", SPIE Proceeding, Infrared Technology, pp. 755-766, Vol. 2552, 1995.

13. M. Z. Tidrow, J. C. Chiang, Sheng S. Li, and K. Bacher, "A high strain two-stack two-color quantum well infrared photodetector", Appl. Phys. Lett. **70**, 859 (1997).